Analysis of high-pressure Diesel fuel injection processes using LES with real-fluid thermodynamics and transport

Guilhem Lacaze,[a] Antony Misdariis,[b] Anthony Ruiz,[a]
and Joseph C. Oefelein[a]

[a] *Combustion Research Facility, Sandia National Laboratories, Livermore, CA 94551-0969 USA*

[b]*Renault SAS, 1 Avenue Cornuel, 91570 Lardy, France*

Corresponding Author:

Guilhem Lacaze

Combustion Research Facility
Sandia National Laboratories
7011 East Avenue, Mail stop 9051,
Livermore, CA 94551-0969 USA

Tel: (925) 294-6058
Fax: (925) 294-3055
Email: *gnlacaz@sandia.gov*

Name of Colloquium: Spray and Droplet Combustion

Total Length of Paper: 5797 words (obtained using method 2, LaTeX two-column procedure).
Main text, equations and acknowledgements: 2950
Nomenclature: 0
References: 736
Figures: $344 + 556 + 143 + 450 + 152 + 136 + 330 = 2111$
Tables: 0

The Authors agree to pay color reproduction charges.

Submitted for presentation at the
35th International Symposium on Combustion
San Francisco, USA, August 03 – 08, 2014

Analysis of high-pressure Diesel fuel injection processes using LES with real-fluid thermodynamics and transport

Guilhem Lacaze,[a,*] Antony Misdariis,[b] Anthony Ruiz,[a] Joseph C. Oefelein[a]

[a] *Combustion Research Facility, Sandia National Laboratories, Livermore, CA 94551, USA*
[b] *Renault SAS, 1 Avenue Cornuel, 91570 Lardy, France*
** Corresponding author: gnlacaz@sandia.gov*

Abstract

Imaging has long shown that under some high-pressure conditions, the presence of discrete two-phase flow processes becomes diminished. Instead, liquid injection processes transition from classical sprays to dense-fluid jets with no drops present. When and how this transition occurs, however, was not well understood until recently. In this paper, we summarized a new theoretical description that quantifies the effects of real fluid thermodynamics on liquid fuel injection processes as a function of pressure at typical Diesel engine operating conditions. We then apply the Large Eddy Simulation (LES) technique coupled with real-fluid thermodynamics and transport to analyze the flow at conditions when cylinder pressures exceed the thermodynamic critical pressure of the injected fuel. To facilitate the analysis, we use the experimental data posted as part of the Engine Combustion Network (see www.sandia.gov/ECN); namely the "Spray-A (n-dodecane)" case. Calculations are performed by rigorously treating the experimental operating conditions and relevant thermo-physical gas-liquid mixture properties. Details related to the transient mixing field are presented with emphasis on the state of the mixing field prior to auto-ignition. The analysis reveals the profound effect of supercritical fluid phenomena on the instantaneous three-dimensional structure of the compressed liquid core and related multicomponent mixing layer dynamics.

Keywords: LES; Diesel fuel injection; Supercritical fluids; Real-fluid thermodynamics

1. Introduction

Future Diesel engines will operate in high pressure, low temperature regimes with significantly optimized fuel injection systems. As such, the current research is focused on developing a better understanding of fuel mixing at elevated pressures and the related transient mixing mechanisms. Research over the past decade has provided significant insights into the structure and dynamics of multiphase flows at high pressures (see for example [1–5]). Most of this research has been done in the context of liquid-rocket propulsion, which involves direct injection of both liquid fuel and oxidizer into the combustion chamber. However, the observed trends are equally valid for other liquid fueled devices. Here we focus on Diesel engines at conditions where the fuel is injected at conditions that exceed its thermodynamic critical pressure. In particular, recent research by Dahms and Oefelein [6, 7] has provided new conceptual insights into Diesel injection processes at high-pressures.

Imaging has long shown that under some high-pressure conditions, the presence of discrete two-phase flow processes becomes diminished. Under such conditions, liquid injection processes transition from classical sprays to dense-fluid jets with no drops present. When this transition occurs, however, was not well understood until recently. To the Author's knowledge, the theory presented in References [6, 7] is the first to quantify this transition. A key output are regime diagrams such as the example shown in Fig. 1. Detailed analysis of the gas-liquid interfacial structure quantifies under what conditions "classical" spray dynamics transition to diffusion dominated mixing. Predictions have been corroborated using microscopic imaging to visualize the features of dense-fluid jets (top right image in Fig. 1) and classical spray atomization (bottom right image). Analysis of the trends suggests that most high-performance combustion devices currently operate over ranges of pressures and temperatures in the vicinity of this transitional regime.

The regime diagram in Fig. 1 shows results for n-dodecane injected at a temperature of $363\ K$ into gaseous nitrogen at varying ambient pressures and temperatures. The classical spray regime (highlighted in white) and diffusion-dominated mixing regime (gray) are found using the Knudsen-number criterion explained in Reference [7]. To illustrate the relevance of this diagram, ambient gas pressure-temperature lines, which span a range of conditions during different Diesel engine compression cycles, are shown for three representative conditions; a) turbo-charged, b) medium-load, and c) light-load operation. The corresponding initial pressures and temperatures are a) $2.5\ bar$, $363\ K$, b) $1.6\ bar$, $343\ K$, and c) $1\ bar$, $335\ K$, respectively. Fuel injection then occurs at full compression conditions, as indicated by the three respective points in the diagram. Interestingly, the cylinder pressures at full compression exceed the supercritical mixture pressure for all of the cases considered. Only under representative light-load operation does there appear to be a chance that classical fuel spray atomization takes place. Thus, contrary to conventional wisdom, the regime diagram suggests that classical spray phenomena does not occur at typical Diesel injection conditions. Instead, the fuel jet exhibits diminished interfacial structure and surface tension, which leads to diffusion-dominated mixing.

To enhance our understanding of the processes described above, we have combined the new theoretical findings and the Large Eddy Simulation (LES) technique to gain a more detailed view into direct injection processes in Diesel engines. At the conditions of interest, mixing layer dynamics are dominated by non-ideal thermodynamics and transport processes. We use the experimental data provided by Pickett *et al.* as part of the Engine Combustion Network cases (see www.ca.sandia.gov/ECN [8]); namely, the “Spray-A (n-dodecane)” case. This case corresponds identically to the conditions depicted by the dense-fluid jet image shown at the top right in Fig. 1. LES is performed using the real-fluid model describe below. Results are then analyzed from the perspective of real-fluid thermodynamics with emphasis on the state of the transient mixing field prior to auto-ignition.

2. Approach

LES is performed using a single unified code framework called RAPTOR, which is a fully compressible solver that has been optimized to meet the strict algorithmic requirements imposed by the LES formalism. The theoretical framework solves the fully coupled conservation equations of mass, momentum, total-energy, and species for a chemically reacting flow. It is designed to handle high Reynolds number, high-pressure, real-gas and/or liquid conditions over a wide Mach operating range. It also accounts for detailed thermodynamics and transport processes at the molecular level, and is sophisticated in its ability to handle a generalized model framework. A noteworthy aspect of RAPTOR is it was designed specifically for LES using non-dissipative, discretely conservative, staggered, finite-volume differencing. This eliminates numerical contamination of the subgrid-scale models due to artificial dissipation and provides discrete conservation of mass, momentum, energy, and species, which is an imperative requirement for high quality LES. Details related to the baseline formulation and subgrid-scale models are given by Oefelein [9]. Representative case studies are given by Oefelein *et al.* [10–13, 15–18].

The baseline system of equations are cast in dimensionless form using a reference length-scale δ_{ref}, flow speed U_{ref}, and fluid state characterized by a reference density ρ_{ref}, sound speed c_{ref}, constant pressure specific heat $C_{p_{\mathrm{ref}}}$, and dynamic viscosity μ_{ref}. Using these quantities, reference Mach and Reynolds numbers are defined as $M = U_{\mathrm{ref}}/c_{\mathrm{ref}}$ and $Re = \rho_{\mathrm{ref}} U_{\mathrm{ref}} \delta_{\mathrm{ref}}/\mu_{\mathrm{ref}}$. With these definitions, the filtered conservation equations of mass, momentum, total-energy and chemical species can be written in conservative form as follows:

$$\frac{\partial \overline{\rho}}{\partial t} + \nabla \cdot (\overline{\rho} \tilde{\mathbf{u}}) = 0, \tag{1}$$

$$\frac{\partial}{\partial t}(\overline{\rho} \tilde{\mathbf{u}}) + \nabla \cdot \left[\left(\overline{\rho} \tilde{\mathbf{u}} \otimes \tilde{\mathbf{u}} + \frac{\mathcal{P}}{M^2} \mathbf{I} \right) \right] = \nabla \cdot \vec{\vec{\mathcal{T}}}, \tag{2}$$

$$\frac{\partial}{\partial t}(\overline{\rho} \tilde{e}_t) + \nabla \cdot [(\overline{\rho} \tilde{e}_t + \mathcal{P}) \tilde{\mathbf{u}}] = \nabla \cdot \left[\left(\vec{\mathcal{Q}}_e + M^2 (\vec{\vec{\mathcal{T}}} \cdot \tilde{\mathbf{u}}) \right) \right] + \overline{\dot{Q}}_e, \tag{3}$$

$$\frac{\partial}{\partial t}(\overline{\rho} \tilde{Y}_i) + \nabla \cdot (\overline{\rho} \tilde{Y}_i \tilde{\mathbf{u}}) = \nabla \cdot \vec{\mathcal{S}}_i + \overline{\dot{\omega}}_i. \tag{4}$$

The terms $\mathcal{P}$, $\vec{\vec{\mathcal{T}}}$, $\vec{\mathcal{Q}}_e$ and $\vec{\mathcal{S}}_i$ represent respective composite (i.e., molecular plus subgrid-scale) stresses and fluxes. The terms $\overline{\dot{Q}}_e$ and $\overline{\dot{\omega}}_i$ represent the filtered energy and species source terms.

The subgrid-scale closure is obtained using the "mixed" dynamic Smagorinsky model by combining the models proposed by Erlebacher *et al*. [19] and Speziale [20] with the dynamic modeling procedure [21–25]. The composite stresses and fluxes in Eqs. (1)–(4) are then given as:

$$\begin{aligned} \vec{\vec{\mathcal{T}}} &= (\mu_t + \mu)\frac{1}{Re}\left[-\frac{2}{3}(\nabla \cdot \tilde{\mathbf{u}})\mathbf{I} + \left(\nabla\tilde{\mathbf{u}} + \nabla\tilde{\mathbf{u}}^T\right)\right] \\ &\quad -\overline{\rho}\left(\widetilde{\tilde{\mathbf{u}} \otimes \tilde{\mathbf{u}}} - \tilde{\tilde{\mathbf{u}}} \otimes \tilde{\tilde{\mathbf{u}}}\right), \end{aligned} \tag{5}$$

$$\begin{aligned} \vec{\mathcal{Q}}_e &= \left(\frac{\mu_t}{Pr_t} + \frac{\mu}{Pr}\right)\frac{1}{Re}\nabla\tilde{h} + \sum_{i=1}^{N}\tilde{h}_i\vec{\mathcal{S}}_i \\ &\quad -\overline{\rho}\left(\widetilde{\tilde{h}\tilde{\mathbf{u}}} - \tilde{\tilde{h}}\tilde{\tilde{\mathbf{u}}}\right), \text{ and} \end{aligned} \tag{6}$$

$$\vec{\mathcal{S}}_i = \left(\frac{\mu_t}{Sc_{t_i}} + \frac{\mu}{Sc_i}\right)\frac{1}{Re}\nabla\tilde{Y}_i - \overline{\rho}\left(\widetilde{\tilde{Y}_i\tilde{\mathbf{u}}} - \tilde{\tilde{Y}}_i\tilde{\tilde{\mathbf{u}}}\right). \tag{7}$$

The term μ_t represents the subgrid-scale eddy viscosity given by

$$\mu_t = \overline{\rho}C_R\Delta^2\Pi_{\tilde{\mathbf{S}}}^{\frac{1}{2}}, \tag{8}$$

where

$$\Pi_{\tilde{\mathbf{S}}} = \tilde{\mathbf{S}} : \tilde{\mathbf{S}}, \text{ and } \tilde{\mathbf{S}} = \frac{1}{2}\left(\nabla\tilde{\mathbf{u}} + \nabla\tilde{\mathbf{u}}^T\right). \tag{9}$$

The terms C_R, Pr_t, and Sc_{t_i} represent the modified Smagorinsky, subgrid-scale Prandtl, and subgrid-scale Schmidt numbers, respectively, and are evaluated dynamically as functions of space and time. The overall model includes the Leonard and cross-term stresses and provides a Favre averaged generalization of the Smagorinsky eddy viscosity model [26] coupled with gradient diffusion models to account for subgrid-scale mass and energy transport processes.

Equations (1)–(4) coupled with an appropriate equation of state, appropriate treatments of thermodynamic and transport properties, and validated mixing and combining rules accommodate the most general system of interest including cases when multicomponent and/or preferential diffusion processes are present. The property evaluation scheme used for the current study is designed to account for thermodynamic non-idealities and transport anomalies over a wide range of pressures and temperatures. The scheme is comprehensive and intricate, thus only a skeletal description can be given here. The extended corresponding states model [27, 28] is employed with a cubic equation of state. Experience has shown that both the Soave-Redlich-Kwong (SRK) and Peng-Robinson (PR) equations, when used in conjunction with the corresponding states principle, can give accurate results over the range of pressures, temperatures, and mixture states of interest here. The SRK coefficients are adjusted to fit vapor pressure data and are thus more suitable for conditions when the reduced temperature is less than one. The PR coefficients, on the other hand, are more suitable for conditions when the reduced temperature is greater than one. Here the PR equation of state was used exclusively.

A summary of the cubic equations of state and recommended constants is given by Reid *et al*. [29, Chapter 3]. Having established an analytical representation for real mixture pressure-volume-temperature (PVT) behavior, the thermodynamic properties are obtained in two steps. First, respective component properties are combined at a fixed temperature using the extended corresponding states methodology to obtain the mixture state at a given reference pressure. A pressure correction is then applied using departure functions of the form given by Reid *et al*. [29, Chapter 5]. These functions are exact relations derived using the Maxwell relations (e.g., see VanWylen and Sonntag [31, Chapter 10]) and make full use of the real mixture PVT path dependencies dictated by the equation of state. Standard state properties are obtained using the databases developed by Gordon and McBride [32] and Kee *et al*. [33]. Molecular transport properties are evaluated in a manner analogous to the thermodynamic properties. Viscosity and thermal conductivity are obtained using the extended corresponding states methodologies developed by Ely and Hanley [34]. Mass and thermal diffusion coefficients are obtained using the methodologies outlined by Bird *et al*. [35] and Hirschfelder *et al*. [36] in conjunction with the corresponding states methodology proposed by Takahashi [37].

3. Results and Discussion

Using LES with the real-fluid model framework described above, we have performed a series of studies aimed at understanding the diffusion dominated mixing phenomena illustrated in Fig. 1. We focus on the Spray-A experiment described by Pickett *et al*. [8]. Liquid n-dodecane at $363\ K$ is injected through a $0.09\ mm$ diameter injector nozzle into a gaseous mixture at $900\ K$ and $60\ bar$. These are precisely the same conditions represented by the dense-fluid jet image shown at the top right in Fig. 1. The peak injection velocity is $620\ m/s$, which was selected to provide the same injected mass flow rate as the experiment. A synthetic turbulent signal with a turbulent intensity of 5-percent is superimposed on the bulk profile. Measurements have shown that the vessel temperature is almost uniform in space, which justifies the use of adiabatic walls in the simulation. The grid spacing in the vicinity of the injector exit is approximately $4\ \mu m$, with the grid stretched optimally in the downstream and radial directions. The integration time step is $2.3\ ns$.

Figure 2 shows a qualitative comparison of the injection sequence. Results from the LES are compared to the shadowgraphs from Pickett *et al*. [38]. The experimental images were obtained using a diffuser back illumination method, with the dense region highlighted using an arbitrary cut-off value in the gray scale. Based on recommendations from Picket *et al*., instantaneous shots of the LES temperature field were chosen for comparisons. Comparisons between respective images shows qualitatively good agreement between the experiment and LES. Large structures present in the back-illumination images are also observed in the numerical results. The density of the n-dodecane jet is slightly above $700\ kg/m^3$ at the injector nozzle exit whereas the density of the ambient gas is $23\ kg/m^3$. The presence of strong density gradients is known to have a stabilization effect on hydrodynamic instabilities [30], which delays the destabilization of the jet. Once destabilization occurs, parcels of dense fluid detach from the compressed liquid jet. The dense fragments can still be observed 70 diameters ($6.3\ mm$) downstream of the injector exit. The presence of these fast-moving structures enhances local turbulence. The eddies generated in the shear layers significantly affects mixing.

The vapor and "liquid" penetration trajectories are shown in Fig. 3. In the LES, vapor penetration is detected by the most upstream point of the iso-surface characterized by a mixture fraction of $Z = 0.01$. The sensitivity of this value has been tested and penetration curves have less than 2-percent variation between $Z = 0.01$ and $Z = 0.1$. LES results are in good agreement with experimental measurements, except at the initial phase of injection ($t < 50\ \mu s$). During the initial startup, the simulated vapor penetration is slightly over-predicted. This is possibly an artifact of boundary anomalies associated with the interior sac and nozzle regions of the injector. The time-resolved liquid core length was determined from high-speed Mie-scatter imaging using a 3-percent threshold of maximum intensity, which to some degree is an arbitrary value. Given the current premise that a distinct gas-liquid interface does not exist in this flow, defining the threshold associated with the compressed-liquid core requires additional analysis. Two liquid penetration curves are extracted from the LES to investigate. The first is based on a threshold of $Z = 0.79$, which is the value where the density changes the most with respect to Z (see Fig. 4 b). The second was based on a threshold of $Z = 0.6$, which is simply the value that provides the best match with the experimental data. Both thresholds lead to the same trend as in the experiment. A plateau is observed in the temporal evolution with differing constant values of penetration depending on the mixture fraction value chosen.

A key focal point of this study is to better understand the local instantaneous mixture state of the jet immediately prior to auto-ignition, which occurs at approximately $t = 260\ \mu s$ after the start of injection. Figure 4 provides a global representation of the mixture state at this point in time. Scatter plots of (a) temperature, (b) density, (c) compressibility factor, (d) Mach number, and (e) speed of sound are shown as a function of mixture fraction. The adiabatic mixing temperature is also plotted in Fig. 4(a), as shown by the blue solid line. The red line represents the average. The non-linear relation between these quantities and mixture fraction can be largely attributed to real-gas thermodynamics, where large changes in temperature and density occur as a function of relatively small variations in composition. Scatter away from near adiabatic mixing can be attributed to multidimensional transport anomalies. Turbulent stretching and curvature induced by the evolving coherent structures amplifies preferential diffusion effects at both resolved- and subgrid-scales.

Figure 4(d) and (e) reveal new and interesting conditions associated with real-fluid thermodynamics coupled with turbulent mixing: the Mach number in the flow varies from low-subsonic levels to approximately Mach 2.5. The speed of sound ($c = \sqrt{\gamma(\partial P/\partial \rho)_{T,Y_i}}$) is seen to vary from approximately $600\ m/s$ in the ambient gas, to $200\ m/s$ at a mixture fractions of approximately $Z = 0.79$, to $1000\ m/s$ in the pure fuel. In the mixing layer of the jet, non-linear thermodynamic effects lead to an increase in the ratio of specific heats and a significant decrease of the partial derivative $(\partial P/\partial \rho)_{T,Y_i}$ which globally results in strong decrease of the sound speed. In the same region, the entrainment caused by the high-speed jet induces flow velocities of approximately $400\ m/s$, which is more than two times the local sound speed. These localized regions of supersonic flow have a significant influence on the local pressure field and resultant scalar mixing processes.

To better understand the state of the transient mixing field just prior to auto-ignition, one can use the parametrization shown in Fig. 4 to approximate local ignition delay times in the mixture. The adiabatic mixing temperature is discretized in mixture fraction space, as shown with the red line in Fig. 4(a). A Perfectly Stirred Reactor (PSR) simulation is performed at each of these points using CANTERA [39] and the detailed scheme developed by Westbrook *et al.* [40]. The chemical kinetics scheme is composed of 15787 reactions and 2115 species. Figure 5 shows the type of data obtained. Temperature as a function of time for mixture fractions close to the stoichiometric value of $Z_{\text{st}} = 0.045$ are shown. As is consistent with experimental studies [14], a two-stage ignition process is observed. The auto-ignition time is defined as that needed for the PSR to reach 90-percent of its equilibrium temperature. Figure 6 shows the resulting auto-ignition time as a function mixture fraction. A fourth order polynomial is used to fit the data points located near the stoichiometric point where the auto-ignition time is less than $2.5\ ms$. This allows the auto-ignition field to be mapped over the mixture fraction field.

Using the results obtained above, we now show regions where auto-ignition is most likely to occur. Figure 7(a) shows the ignition delay time, (b) the magnitude of the mixture fraction gradient, (c) the magnitude of the axial-component of velocity, and (d) the typical location where the first ignition kernels are observed in the experiment. Analysis of the temporal evolution of the these fields reveals that regions of the flow that are both flammable and have low values of scalar dissipation rate only appear after approximately $200\ \mu s$ after the start of injection. Thus, the instantaneous flow structure at $260\ \mu s$ was selected to highlight where the ignition delay time is less than $2.5\ ms$. This allows us to focus on the structure of the chemically active regions. These data show that there are many favorable locations that trigger chemical reactions within the mixing layer of the jet. Upstream locations before 200 diameters ($18\ mm$) is where small pockets of flammable mixture appear first. However, Figs. 7(b) and (c) show that strong velocity and mixture fraction gradients in these regions will prohibit the formation of the first flame kernels due to high stretch and scalar dissipation rate. Low gradients and larger flammable pockets are present between 200 and 250 diameters ($18 - 22.5\ mm$) downstream of the injector, which is in qualitative agreement with the location of the initial kernels observed in the experiment. These findings represent a first step toward the development of a robust ignition model based on an appropriately reduced version of the Westbrook *et al.* [40] mechanism.

4. Conclusions

Imaging has long shown that under some high-pressure conditions, the presence of discrete two-phase flow processes becomes diminished. Under such conditions, liquid injection processes transition from classical sprays to dense-fluid jets, with no drops present. When and how this transition occurs, however, was not well understood until recently. In this paper, we have summarized a new theoretical description that quantifies the effects of real fluid thermodynamics on liquid fuel injection processes as a function of pressure at typical Diesel engine operating conditions. We then focused on the effects of real-fluid thermodynamics and transport using the Large Eddy Simulation (LES) technique. Analysis was performed using the Engine Combustion Network (www.sandia.gov/ECN) Spray-A case. LES was performed by identically matching the operating conditions used in the experiments. Results were analyzed with emphasis placed on the state of the transient mixing field prior to auto-ignition.

The LES results revealed the instantaneous three-dimensional structure of the injected fuel jet with a degree of resolution that is not accessible by current experimental diagnostics. Using the detailed information available in the LES, results complementing experimental data are shown. Corresponding mixture fraction, temperature, density, Mach number, and speed of sound distributions were analyzed. Large density gradients associated with the compressed liquid core triggers a cascade of processes characteristic of supercritical flows, where turbulent mixing is profoundly modified by high-pressure non-linear mixing and diffusion. Once the destabilization of the dense core occurs, parcels of dense fluid detach. The presence of these fast-moving dense structures enhances local turbulence. An unexpected feature of the present case was how the instantaneous Mach number field varied within the jet mixing layers. Results demonstrated that the flow is supersonic at various locations within the mixing layers due to variations associated with the speed of sound. This remarkable behavior is the result of near supersonic injection of a compressed liquid at supercritical conditions. The subsequent compressibility effects lead to pressure waves that affect the destabilization and transient mixing of the injected fuel.

The present work also focused on the identification of the flammable regions resulting from the present non-ideal mixing. Using the observation that the scatter of temperature in mixture fraction space is small, a series of perfectly-stirred-reactors were computed to generate a mapping of ignition delay time as a function of mixture fraction. This provided an accurate way to localize potentially reactive mixtures. Analysis of the gradients of mixture fraction and velocity showed that a large region of flammable mixture with low gradients forms between 200 and 250 diameters ($18 - 22.5\ mm$) downstream of the injector. In this region, any initial kernel would experience minimum heat losses and stretching. It is in this zone that ignition is observed experimentally. These findings represent a first step toward the development of a robust ignition model based on an appropriately reduced chemical mechanism and related combustion closure.

Acknowledgments

Support for this research was provided jointly by the U. S. Department of Energy; Office of Science (SC), Basic Energy Sciences (BES) program; and the Office of Energy Efficiency and Renewable Energy (EERE), Vehicle Technologies (VT) program, under grant numbers KC0301020 and VT0401000. Development of the foundational property evaluation schemes for multicomponent hydrocarbon mixtures was supported by the SC-BES program. Application of these tools to advanced engine combustion simulations was supported by the EERE-VT program. Sandia National Laboratories is a multiprogram laboratory operated by Sandia Corporation, a Lockheed Martin Company, for the United States Department of Energy under contract DE-AC04-94-AL85000. This research used resources of the Oak Ridge Leadership Computing Facility located in the Oak Ridge National Laboratory, which is supported by the Office of Science under Contract DE-AC05-00OR22725.

References

[1] J. C. Oefelein, V. Yang, *Combustion Science and Technology* 178 (1-3) (2006) 1–621, 20 Topical Papers.
[2] L. C. Selle, N. A. Okong'o, J. Bellan, K. G. Harstad, *Journal of Fluid Mechanics* 593 (2007) 57–91.
[3] G. Ribert, N. Zong, V. Yang, L. Pons, N. Darabiha, S. Candel, *Combustion and Flame* 154 (2008) 319–330.
[4] G. Lacaze, B. Cuenot, T. Poinsot, M. Oschwald, *Combustion and Flame* 156 (2009) 1166–1180.
[5] T. Schmitt, Y. Méry, M. Boileau, S. Candel, *Proceedings of the Combustion Institute* 33 (2011) 1383–1390.
[6] R. N. Dahms, J. Manin, L. M. Pickett, J. C. Oefelein, *Proceedings of the Combustion Institute* 34 (2013) 1667–1675, doi: 10.1016/j.proci.2012.06.169.
[7] R. N. Dahms, J. C. Oefelein, *Physics of Fluids* 25 (092103) (2013) 1–24, doi: 10.1063/1.4820346.
[8] L. M. Pickett, *Engine Combustion Network*, www.sandia.gov/ECN, Sandia National Laboratories, Combustion Research Facility, Livermore, California (2005-2013).
[9] J. C. Oefelein, *Progress in Aerospace Sciences* 42 (1) (2006) 2–37.
[10] J. C. Oefelein, *Proceedings of the Combustion Institute* 30 (2005) 2929–2937.
[11] J. C. Oefelein, R. W. Schefer, R. W. Barlow, *AIAA Journal* 44 (3) (2006) 418–433.
[12] J. C. Oefelein, V. Sankaran, T. G. Drozda, *Proceedings of the Combustion Institute* 31 (2007) 2291–2299.
[13] T. C. Williams, R. W. Schefer, J. C. Oefelein, C. R. Shaddix, *Review of Scientific Instruments* 78 (3) (2007) 035114–1–9, doi: 10.1063/1.27.12936.
[14] M. Tanabe, T. Bolik, C. Eigenbrod, H. J. Rath, J. Sato, M. Kono, *Proceedings of the Combustion Institute* 26 (1) (1996) 1637 – 1643.
[15] J. C. Oefelein, G. Lacaze, *Proceedings of the 23rd International Colloquium on the Dynamics of Explosions and Reactive Systems*Irvine, California.
[16] J. C. Oefelein, R. N. Dahms, G. Lacaze, *SAE International Journal of Engines* 5 (3) (2012) 1–10, doi: 10.4271/2012-10-1258.
[17] J. C. Oefelein, R. N. Dahms, G. Lacaze, J. L. Manin, L. M. Pickett, *Proceedings of the 12th International Conference on Liquid Atomization and Spray Systems*Heidelberg, Germany. ISBN 978-88-903712-1-9.
[18] J. C. Oefelein, *Proceedings of the 8th Joint Meeting of the US Sections of the Combustion Institute, Invited Plenary Presentation and Paper*Park City, Utah.
[19] G. Erlebacher, M. Y. Hussaini, C. G. Speziale, T. A. Zang, *Journal of Fluid Mechanics* 238 (1992) 155–185.
[20] C. G. Speziale, *Journal of Fluid Mechanics* 156 (1985) 55–62.
[21] M. Germano, U. Piomelli, P. Moin, W. H. Cabot, *Physics of Fluids* 3 (7) (1991) 1760–1765.
[22] P. Moin, K. Squires, W. Cabot, S. Lee, *Physics of Fluids* 3 (11) (1991) 2746–2757.
[23] D. K. Lilly, *Physics of Fluids* 3 (11) (1992) 633–635.
[24] Y. Zang, R. L. Street, J. R. Koseff, *Physics of Fluids* 5 (12) (1993) 3186–3195.
[25] B. Vreman, B. Geurts, H. Kuerten, *Physics of Fluids* 6 (12) (1994) 4057–4059.
[26] J. Smagorinsky, *Monthly Weather Review* 91 (1963) 99–164.
[27] T. W. Leland, P. S. Chappelear, *Industrial and Engineering Chemistry Fundamentals* 60 (7) (1968) 15–43.
[28] J. S. Rowlinson, I. D. Watson, *Chemical Engineering Science* 24 (8) (1969) 1565–1574.
[29] R. C. Reid, J. M. Prausnitz, B. E. Polling, *The Properties of Liquids and Gases*, 4th Edition, McGraw-Hill, New York, New York, 1987.
[30] I. A. Hannoun, H. J. S. Fernando, E. J. List, *Journal of Fluid Mechanics* 189 (1988) 189–209.
[31] G. J. VanWylen, R. E. Sonntag, *Fundamentals of Classical Thermodynamics*, 3rd Edition, John Wiley and Sons, Incorporated, New York, New York, 1986.
[32] S. Gordon, B. J. McBride, *Computer Program for Calculation of Complex Chemical Equilibrium Compositions, Rocket Performance, Incident and Reflected Shocks and Chapman-Jouguet Detonations*, Tech. Rep. NASA SP-273, National Aeronautics and Space Administration (1971).
[33] R. J. Kee, F. M. Rupley, J. A. Miller, *Chemkin Thermodynamic Data Base*, Tech. Rep. SAND87-8215B, Sandia National Laboratories, supersedes SAND87-8215 dated April 1987 (1990).
[34] J. F. Ely, H. J. M. Hanley, *Industrial and Engineering Chemistry Fundamentals* 20 (4) (1981) 323–332.
[35] R. B. Bird, W. E. Stewart, E. N. Lightfoot, *Transport Phenomena*, John Wiley and Sons, Incorporated, New York, New York, 1960.
[36] J. O. Hirschfelder, C. F. Curtiss, R. B. Bird, *Molecular Theory of Gases and Liquids*, 2nd Edition, John Wiley and Sons, Incorporated, New York, New York, 1964.
[37] S. Takahashi, *Journal of Chemical Engineering of Japan* 7 (6) (1974) 417–420.
[38] L. M. Pickett, C. L. Genzal, J. Manin, L.-M. Malbec, L. Hermant, *Proceedings of the 23rd Annual Conference on Liquid Atomization and Spray Systems*Ventura, California.
[39] D. Goodwin, *Cantera: An Object-Oriented Software Toolkit for Chemical Kinetics, Thermodynamics, and Transport Processes*, http://code.google.com/p/cantera, california Institute of Technology, Pasadena, California (2009).
[40] C. K. Westbrook, W. J. Pitz, O. H. Herbineta, H. J. Currana, E. J. Silkea, *Combustion and Flame* 156 (2009) 181–199, doi: http://dx.doi.org/10.1016/j.combustflame.2008.07.014.

5. *

List of Figures

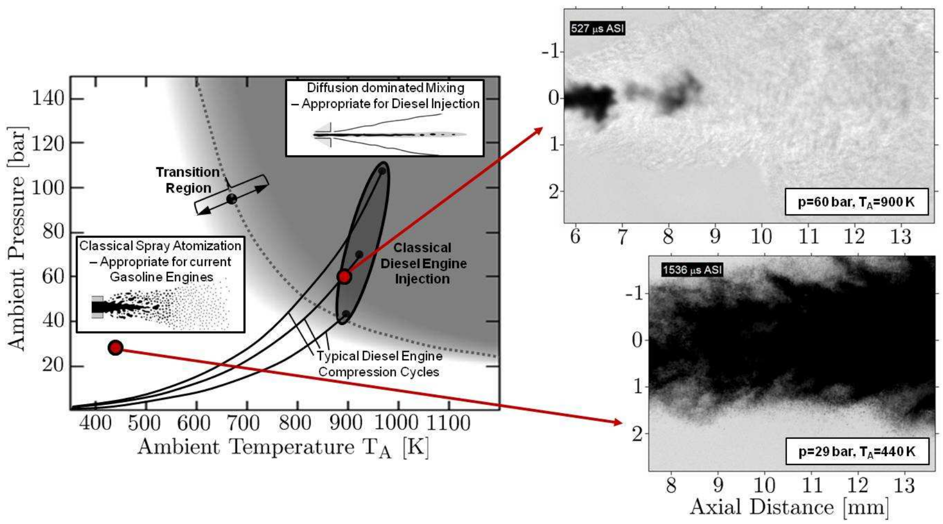

Fig. 1: Regime diagram for n-dodecane injected at a temperature of $363\ K$ into nitrogen suggests the presence of dense supercritical jets under diesel engine conditions without drop formation. High-speed imaging of both a dense jet and spray illustrates the significant transitional change that occurs at high supercritical pressures [6, 7] (Images on right courtesy of L. M. Pickett, Sandia National Laboratories, Combustion Research Facility).

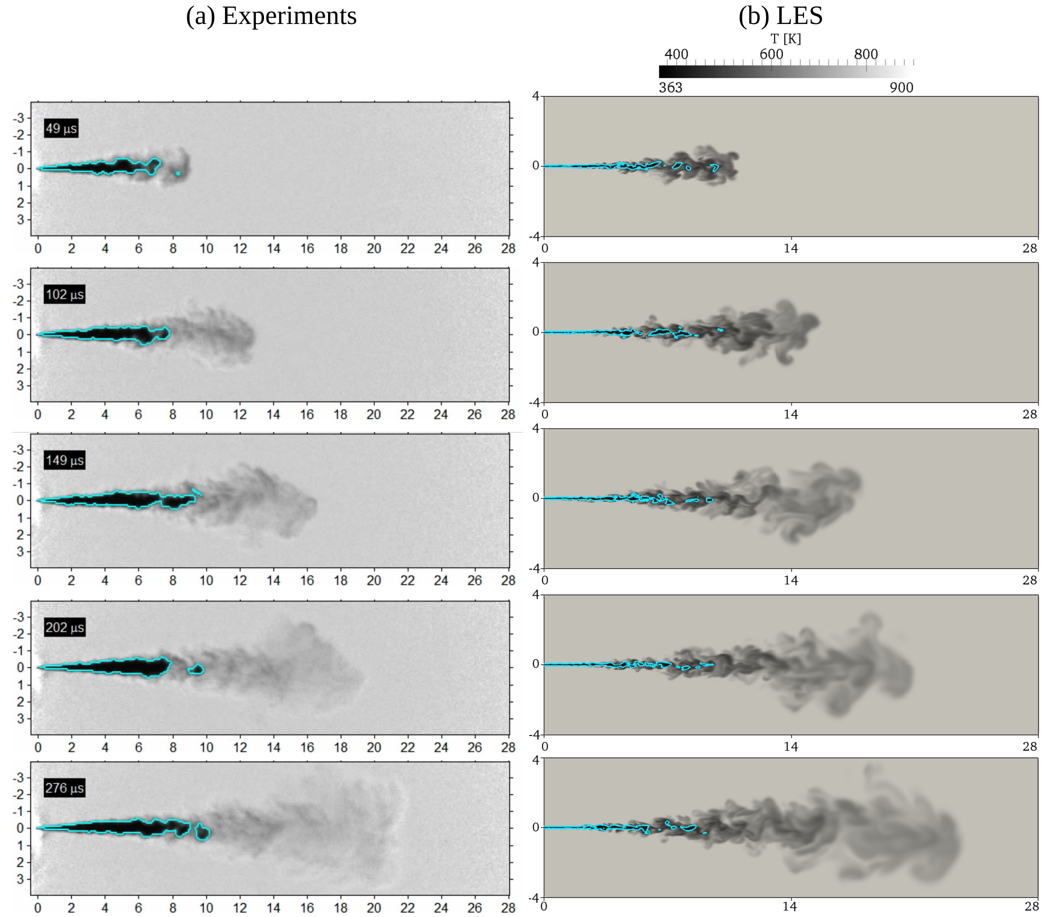

Fig. 2: Injection sequence showing (a) shadowgraphs from Pickett *et al*. [38] and (b) corresponding LES fields. Images are obtained using diffused back illumination with a grayscale intensity threshold set to qualitatively indicate the dense liquid region. Based on recommendations from Picket *et al*., instantaneous shots of the LES temperature field were chosen for comparisons. Spacial graduations are in mm and time is in μs, as indicated in the respective images.

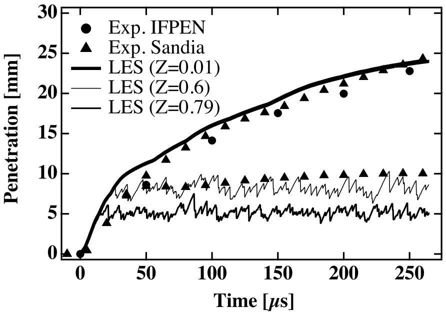

Fig. 3: Vapor and liquid penetration trajectories of the jet. The time-resolved liquid core length was determined from high-speed Mie-scatter imaging using a 3-percent threshold of maximum intensity.

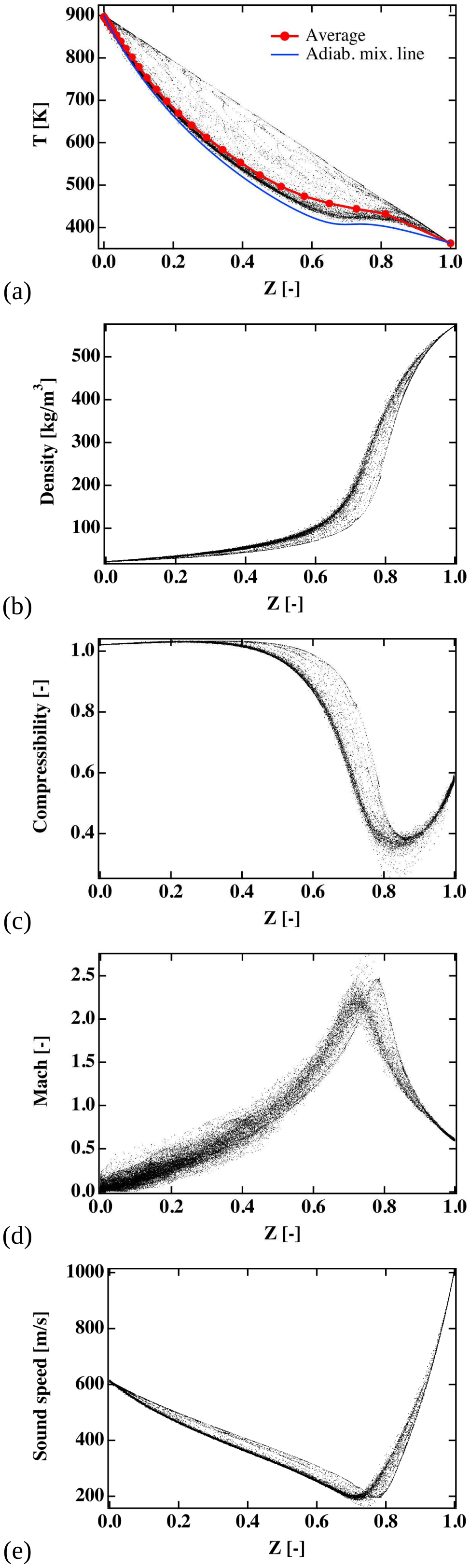

Fig. 4: Scatter plots describing the global mixture state just prior to ignition at $t = 260\ \mu s$.

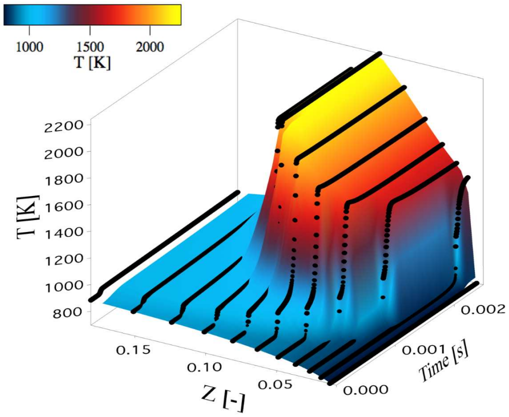

Fig. 5: Ignition delay time along mixing line.

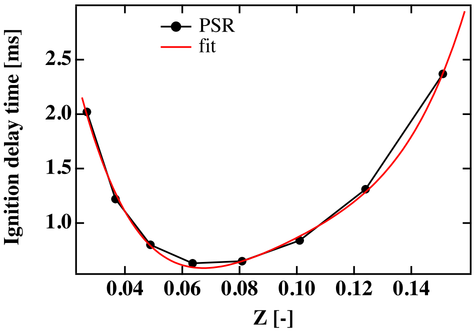

Fig. 6: Mapping of ignition delay time onto mixture fraction. Each point corresponds to a PSR simulation.

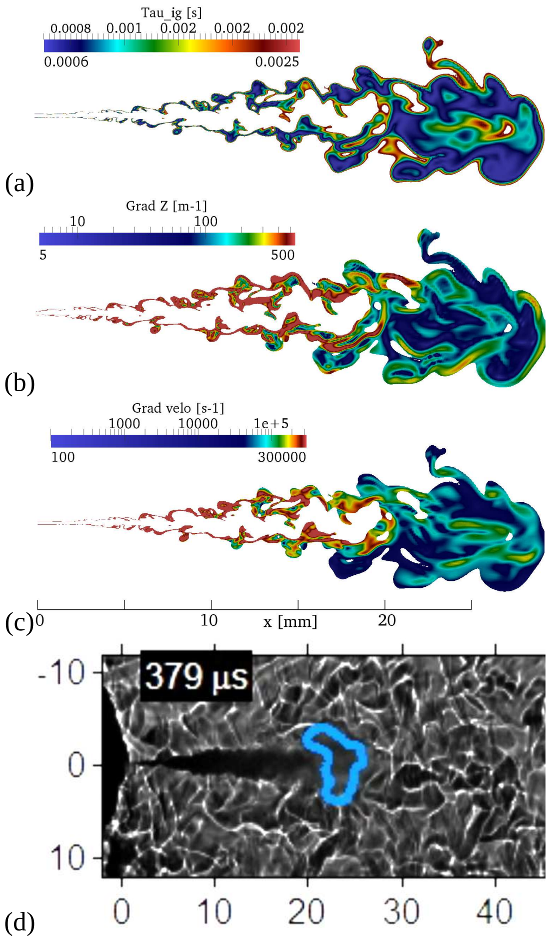

Fig. 7: Instantaneous flow structure close to the ignition time ($260\ ms$) where the ignition delay is less than $2.5\ ms$; (a) ignition delay time, (b) magnitude of mixture fraction gradient, (c) magnitude of axial-component of velocity, and (d) typical location of first ignition kernels in the experiment [38].